Lawrence Berkeley National Laboratory
LBL Publications

Title
Simulation of Gas Production from Multilayered Hydrate-Bearing Media with Fully Coupled Flow, Thermal, Chemical and Geomechanical Processes Using TOUGH+Millstone. Part 3: Production Simulation Results

Permalink
https://escholarship.org/uc/item/4mq51132

Journal
Transport in Porous Media, 129(1)

ISSN
0169-3913

Authors
Reagan, Matthew T
Queiruga, Alejandro F
Moridis, George J

Publication Date
2019-08-01

DOI
10.1007/s11242-019-01283-1

Peer reviewed

Simulation of Gas Production from Multilayered Hydrate Bearing Media with Fully Coupled Flow, Thermal, Chemical and Geomechanical Processes using TOUGH+Millstone: Part 3: Production Simulation Results

Matthew T. Reagan · Alejandro F. Queiruga · George J. Moridis

Abstract The TOUGH+Millstone simulator has been developed for the analysis of coupled flow, thermal and geomechanical processes associated with the formation and/or dissociation of CH_4-hydrates in geological media. It is composed of two constituent codes: (a) a significantly enhanced version of the TOUGH+Hydrate simulator, v2.0, that accounts for all known flow, physical, thermodynamic and chemical processes associated with the evolution of hydrate-bearing systems and includes the most recent physical properties relationships, coupled seamlessly with (b) Millstone v1.0, a new code that addresses the conceptual, computational and mathematical shortcomings of earlier codes used to describe the geomechanical response of these systems. The capabilities of the TOUGH+Millstone code are demonstrated in the simulation and analysis of the system flow, thermal, and geomechanical behavior during gas production from a realistic complex offshore hydrate deposit.

In the third paper of this series, we apply the simulators described in Parts 1 and 2 to a problem of gas production from a complex, multilayered system of hydrate-bearing sediments in an oceanic environment. We perform flow simulations of constant-pressure production via a vertical well, and compare those results to a coupled flow-geomechanical simulation of the same process. The results demonstrate the importance of fully coupled geomechanics when modeling the evolution of reservoir properties during production.

Keywords Methane hydrates · Reservoir Simulation · Geomechanics · Coupled processes

1 Introduction

The TOUGH+HYDRATE (T+H) code (Moridis et al., 2008b) is a simulator developed at the Lawrence Berkeley National Laboratory (LBNL) to model non-isothermal CH_4 release, phase behavior and flow under conditions typical of CH_4-hydrate deposits. T+H is a fully compositional

M. Reagan
Energy Geosciences Division, Lawrence Berkeley National Laboratory, California, United States
E-mail: mtreagan@lbl.gov

A. Queiruga
Energy Geosciences Division, Lawrence Berkeley National Laboratory, California, United States
E-mail: afqueiruga@lbl.gov

G. Moridis
Petroleum Engineering Department, Texas A&M University, United States
Energy Geosciences Division, Lawrence Berkeley National Laboratory, California, United States
E-mail: moridis@tamu.edu; GJMoridis@lbl.gov

simulator, and accounts for heat and up to four mass components (i.e., H_2O, CH_4, CH_4-hydrate, and water-soluble inhibitors such as salts or alcohols) that are partitioned among four possible phases: gas, aqueous liquid, ice, and hydrate. The T+H code can describe all the 15 possible thermodynamic states (phase combinations) of the CH_4+H_2O system and any combination of the three main hydrate dissociation methods: depressurization, thermal stimulation and the effect of inhibitors. It can handle the phase changes, state transitions, strong nonlinearities and steep solution surfaces that are typical of hydrate dissociation problems. Because of the very large computational requirements that are the norm in hydrate problems, both a serial version (Moridis, 2014; Moridis and Pruess, 2014) and a version parallelized for high performance computing (HPC) systems (Zhang et al., 2008) were developed. The original code (Moridis et al., 2008a), continuously updated versions, and the most recent release (Moridis, 2016) have been used for nearly a decade on a wide range of investigations of gas production from hydrates in both oceanic deposits and in accumulations associated with the permafrost.

Due to the strong dependence of the hydrate saturation to the mechanical properties of the sediments, there is the potential for significant geomechanical responses due to hydrate dissociation. Such concerns led to the coupling of the T+H codes with the new Millstone geomechanical simulator. Part 1 of this series describes in detail the formulation and features of the T+H flow simulator. Part 2 describes the formulation of the geomechanical problem and the design of the Millstone v1.0 simulator. In this paper, Part 3, we apply the TOUGH+Millstone simulator to study production from a challenging hydrate reservoir via a vertical well. In Section 2, we describe in detail the simulation methodology and the reservoir system and the production process. In Section 3, we discuss the results of the hydrogeologic and coupled geomechanical-hydrogeological simulations. The conclusions drawn from these studies and future outlook for the three part series are presented in Section 4.

2 Description of the Geologic System

The geologic system in this study is based on a simplified representation of an actual deposit, currently undergoing analysis as part of a larger ongoing study (Moridis et al., 2018; Waite et al., 2018). The geological model in this study uses simplified parameters and geological models from preliminary analyses of the system. The reservoir is composed of three layers of hydrate-bearing sandy sediments (H1, H2, and H3), two hydrate-free interlayers (M1 and M2) of soft oceanic muds, and an silt/sand aquifer (SA) at the base of the hydrate system directly beneath the H3 layer. The depth to the ocean floor and the thicknesses of the various layers are shown in Figure 1. This is a complex variant of a Class 2 setting, in which the H1 and SA layers are overlain and underlain by very-low-permeability (but not impermeable) muds that form the overburden (OB) and underburden (UB), allowing limited flow between the hydrate-bearing layers (HBL) and the top and bottom system boundaries. The ocean floor is the top boundary of the system, and the bottom boundary is set below the UB at a depth of 300 m from the base of the SA layer (see Figure 1), a depth where initial scoping calculations showed that the pressure P and temperature T are likely to remain constant during the time frame of the simulations.

We investigated the performance of a single vertical well completed from the top of the H1 layer to the bottom of the H3 layer. We studied two different cases which both assume angular symmetry of reservoir properties and phase saturations (axisymmetrical around a vertical wellbore). The first (Case R1, the reference case) represents a long-term production test from a single well, with the outer radius of the cylindrical domain at $r_{max} = 2000$ m, corresponding to an open, or constant-conditions, boundary. This radius was determined to be sufficiently large to effect infinite-acting boundary behavior through smaller scoping simulations.

A second case (Case CS1) describes long-term production from a single vertical well in the center of a multi-well field, with a regular pattern and a well spacing of 300 m. We represent this
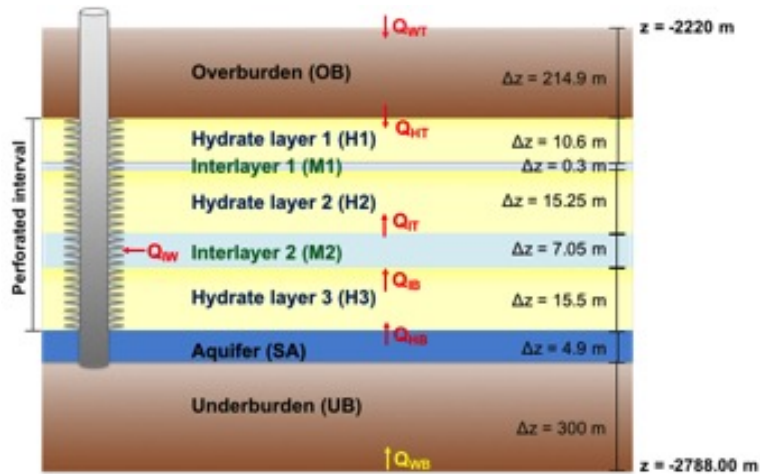
Fig. 1 Geological model and layered geometry of the anonymized reservoir.

by a cylindrical domain with a no-flow boundary at $r_{max} = 150$ m, i.e. a truncated version of the R1 mesh with elements between $r = 150$ m and $r = 2000$ m removed. This assumes that wells in the center of such a field are protected from lateral inflows of water by other adjacent wells with similar production properties (thus the no-flow boundary). This simulation configuration (similar to the familiar "five-spot problem") provides us with an idealized upper-bound on potential single-well productivity within a larger field of wells.

2.1 Domain discretization

The fine discretization used in these simulations are crucial for accurate predictions of the flow and thermal component of the hydrate problem when solid phases such as ice and hydrates are involved. For maximum accuracy, very fine grids were needed for the simulation of production from both vertical well scenarios. In Case R1, the cylindrical domain of the single vertical well problem was discretized into $342 \times 454 = 155,268$ gridblocks in (r, z). In Case CS1, the cylindrical domain was discretized into $342 \times 352 = 120,384$ gridblocks in (r, z). The mesh of Case CS1 is shown in Figure 2. Discretization along the radial direction was non-uniform, increasing logarithmically from r_{well} to r_{max}, with $\Delta r_0 = 0.05$ m. Discretization along the z-axis was nearly-uniform within the reservoir, with $\Delta z = 0.15$ or 0.2 m as dictated by the need to allow the mesh layers to match the known layer thicknesses. The discretization increases outside of the HBL in the muds of the overburden and underburden away from the HBLs, i.e., near the top and bottom of the domain. Full meshing of the overburden and underburden was necessary to accurately describe heat exchange between the HBLs and its boundaries during the endothermic dissociation process that feeds gas production.

Treating hydrate dissociation as an equilibrium reaction and accounting for the effect of the salinity on hydrate dissociation, which resulted in systems of equations with about 620,000 and 480,000 unknowns for Cases R1 and CS1, respectively. The size of the matrices necessitated the use of the parallel version of T+H (Zhang et al., 2008) for the baseline production simulation and sensitivity cases.
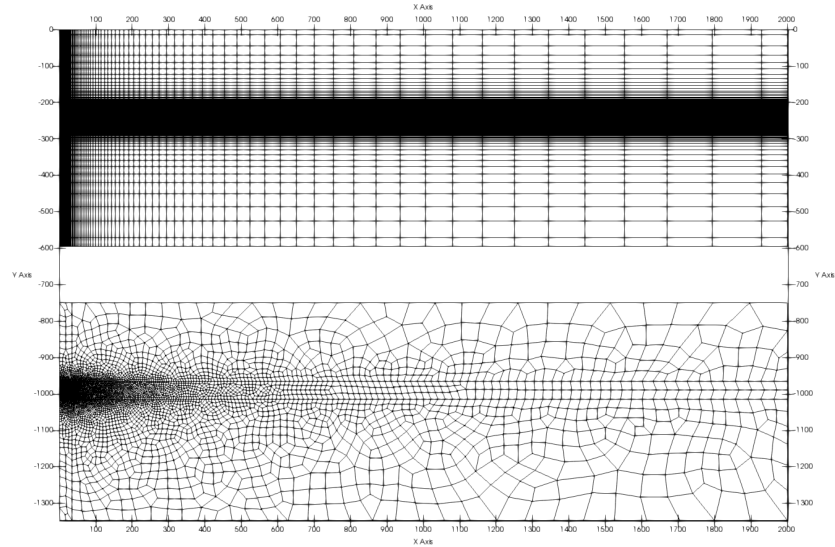
Fig. 2 Meshes used for (top) the thermo-hydrological flow modeling and (bottom) the coupled geomechanical simulation. The mechanical mesh is offset by 750 m downwards in the axis; the meshes are overlaid on top of each other.

2.2 System properties and well description

The hydraulic and thermal properties of the various geological strata are listed in Table 1, and the geomechanical properties of the various layers are listed in Table 2. We assumed that the initial hydrate and aqueous saturations (S_H and S_A, respectively) were uniform throughout the HBLs, and that the mud interlayers, overburden, and underburden had the same properties. In the absence of direct laboratory measurements, the relative permeability, capillary pressure, and the geomechanical relationships and parameters of the sands and muds were based on data from oceanic hydrate deposits in the Ulleung Basin (Moridis et al., 2013).

The wellbore flow was approximated by Darcy flow through a pseudo-porous medium in the interior of the well following earlier studies that confirmed the validity of the approach (Moridis and Reagan, 2007b). This pseudo-medium had $\phi = 1$, a very high $k = 5 \times 10^{-9}$ m^2($= 5.000$ D), a capillary pressure $P_c = 0$, a relative permeability that was a linear function of the phase saturations in the wellbore, and a low (but nonzero) irreducible gas saturation $S_{ir,G} = 0.005$ to allow the emergence of a free gas phase in the well.

2.3 Initial and boundary conditions

We determined the initial conditions in the reservoir by following the initialization process described by Moridis and Reagan (2007a). The uppermost and lowermost gridblock layers, representing the top and bottom of the simulated domain, were assigned time-invariant constant conditions and properties. The temperatures at the top and bottom boundaries from the field data were $T_T =$

Table 1 Properties of the hydrate deposit in Figure 1

Initial pressure at ocean floor (P_T)	2.29×10^7 Pa
Pressure distribution	Hydrostatic
Initial temperature at ocean floor (T_T)	3.46 ^{o}C
Initial temperature at bottom boundary (T_B)	38.335 ^{o}C
Gas composition	100% CH$_4$
Initial saturations in the H1 and H2 HBLs	$S_H = 0.47$
Initial saturations in the H3 HBL	$S_H = 0.73$
Intrinsic permeability k_r of HBLs H1, H2, H3	10^{-12} m^2 (= 1 D); $k_z = 0.01\ k_r$
Porosity ϕ of H1, H2, H3	0.37
Intrinsic permeability kr of M1, M2, SA	10^{-14} m^2 (= 10 mD); $k_z = 0.1\ k_r$
Porosity ϕ of M1, M2, SA	0.37
Intrinsic permeability of OB, UB	5×10^{-19} m^2 (= 50 nD); k_z=0.1 k_r
Porosity ϕ of OB, UB	0.44
Wet and dry thermal conductivity (all layers)	$k_{\theta D} = 0.5$ W/m/K; $k_{\theta w} = 1.16$ W/m/K
Specific heat C_R (all layers)	1000 J/kg/K
Grain density ρ_R (all layers)	2650 kg/m^3
Composite thermal conductivity model	See Part 1
Relative permeability model	$k_{rA} = (S_A^*)^n; k_{rG} = (S_G^*)^m$ $S_A^* = (S_A - S_{irA})/(1 - S_{irA});$ $S_G^* = (S_G - S_{irG})/(1 - S_{irA})$
Relative permeability exponents m, n	$n = 4.3$ (yielding initial $k_{eff} = 10^{-16}$ m$^2 = 0.1$ mD at $S_H = 0.73$ in the H3 HBL); $m = 3.2$
Capillary pressure model (see Part 1)	$P_{cap} = -P_0[(S_A^*)^{(-1/\lambda)} - 1]^\lambda$
P_0 and λ in H1, H2, H3	10^4 Pa; 0.45
S_{irA}, S_{irG} in H1, H2, H3	0.15, 0.01
P_0 and λ in M1, M2, S_A	10^5 Pa; 0.35
S_{irA}, S_{irG} in M1, M2, SA	0.55, 0.03
P_0 and λ in OB, UB	5×10^5 Pa; 0.30
S_{irA}, S_{irG} in OB, UB	0.65, 0.05

Table 2 Geomechanical properties of the hydrate deposit in Figure 1

Young's modulus in H1, H2, H3	$E = 500$ MPa, at $S_H = 0$; $E = 1990$ MPa at $S_H = 1$
Young's modulus in OB, UB, TB, BB, M1, M2, SA	$E = 1096$ MPa
Poisson's ratio in H1, H2, H3	$\nu = 0.4$
Poisson's ratio in OB, TB, UB, BB, M1, M2, SA	$\nu = 0.3$

3.46^oC and $T_B = 38.335^o$C, respectively. Note that the muds in the interlayers, overburden, and underburden were permeable (Table 1), a realistic representation that was consistent with the hydrate system that served as the reference for this study.

Knowing (a) the depth at the base of the HBL, and (b) assuming that the pressures in the subsurface follow the hydrostatic distribution—a hypothesis supported by earlier observations in hydrate accumulations—we determined the pressure P_T (at $z = -2220$ m, see Figure 1) using the $P-$, $T-$, and salinity-adjusted water density, 1005 kg/m^3 at atmospheric pressure. Then we determined the $P-$ and $T-$profiles in the domains and at the bottom boundaries by means of a initialization simulation using P_T and the boundary temperatures T_T and T_B, the hydrostatic gradient, and representative thermal conductivity values. The equilibration simulation was run until thermal, hydrostatic, and chemical equilibrium steady-state conditions were achieved throughout the domain. The results of the equilibration simulation were used as the initial condition for subsequent production simulations.

As concluded and explained in detail by Moridis and Reagan (2007a,b), depressurization appears to be the most effective dissociation strategy. A constant-pressure production method, with a constant bottomhole pressure P_W at the well, is the most promising method of gas production from hydrate deposits because of its simplicity; its technical and economic effectiveness; the response of hydrates to the rapidly propagating pressure wave; the near-incompressibility of water; and the

large heat capacity of water. Constant-rate production is not recommended in this case because the effective permeability k_{eff} at the onset of gas production is very low ($k_{eff} = 1 \times 10^{-16}$ m^2 = 0.1 mD) because of the high initial hydrate saturation S_H and a viable fixed rate cannot be chosen *a priori*. Pure thermal stimulation is an unattractive option because of its limited effectiveness.

Constant-pressure production is performed in T+H by placing an internal boundary in the gridblock above the uppermost cell in the well. By imposing a constant P_W, a zero thermal conductivity $k_\theta = 0$ W/m/K, and a realistic (though unimportant) constant temperature T_W at this internal boundary, the correct constant bottomhole-pressure condition is applied to the well. Non-physical temperature distributions in the well itself are prevented: the large advective flows into the uppermost gridblock from its immediate neighbor eliminate any unrealistic heat transfer effects that could have resulted from an incorrect k_θ and/or T_W. In this study, we use a $P_W = 3.0$ MPa, which exceeds the pressure at the CH$_4$-hydrate quadruple point P_Q, and thus eliminates the possibility of ice formation and corresponding adverse effects on k_{eff}, flow, and production. Flow blockage in the case of combined hydrate and ice presence near the well could potentially cease production.

2.4 Simulation outputs

In the course of the simulation, we monitored the following conditions and parameters: spatial distributions of P, T, and gas and hydrate phase saturations (S_G and S_H); volumetric rates of CH$_4$ released from dissociation and rates of CH$_4$ production at the well (Q_R and Q_P, respectively); cumulative volumes of CH$_4$ released from dissociation, produced at the well, or remaining in the deposit as free gas (V_R, V_P and V_F, respectively); water mass production rate at the well (Q_W) and cumulative mass of produced water (M_W); water-to-gas ratio $R_{WG} = Q_W/Q_P$; and water flows across key boundaries and interfaces.

3 Results

3.1 Gas production and water production in Case R1

Figure 3 shows the time evolution of the rate of gas release from hydrate dissociation, Q_R, and the rate of gas production, Q_P, from the single vertical well at the center of the cylindrical reservoir for Case R1. Several important conclusions can be drawn from Figure 3. First, Q_R and Q_P increase monotonically and reach relatively high levels (> 0.33 ST m^3/d = 106 ST ft^3/d of CH$_4$) at the earliest stages of production. Second, initially $Q_R < Q_P$, indicating that dissolved gas, as opposed to dissociation-originating gas, is a significant contributor to production for the first 300 days, after which time $Q_R > Q_P$. Third, the rate of dissociation is still increasing at the end of the field test timeframe ($t = 540$ d), and as such additional free gas is being released into the HBLs and into the reservoir, and is thus available for future gas production. The high production rate is helped by the relatively elevated initial temperature of the hydrate reservoir, which provides a large reserve of sensible heat to support the endothermic hydrate dissociation reaction.

Following an initial transient spike, the water production rate Q_W in Figure 4 is high and continuously increasing, albeit at a modest rate, during the 540 days of the simulation, indicating that water inflows through the boundaries are progressively facilitated by an increase in the effective permeability of the HBLs as hydrates dissociate. In Case R1, the ratio of water produced to gas produced, $R_{WG} = V_W/V_G$, shown in Figure 4 declines very slowly and persists at very high levels during the simulated production period. Note that R_{WG} in a hydrate system with closed boundaries tends to asymptotically approach values around 4 (Moridis and Reagan, 2007a,b), but here R_{WG} is 18 times larger and would require a significant water management effort if this system were a production target.
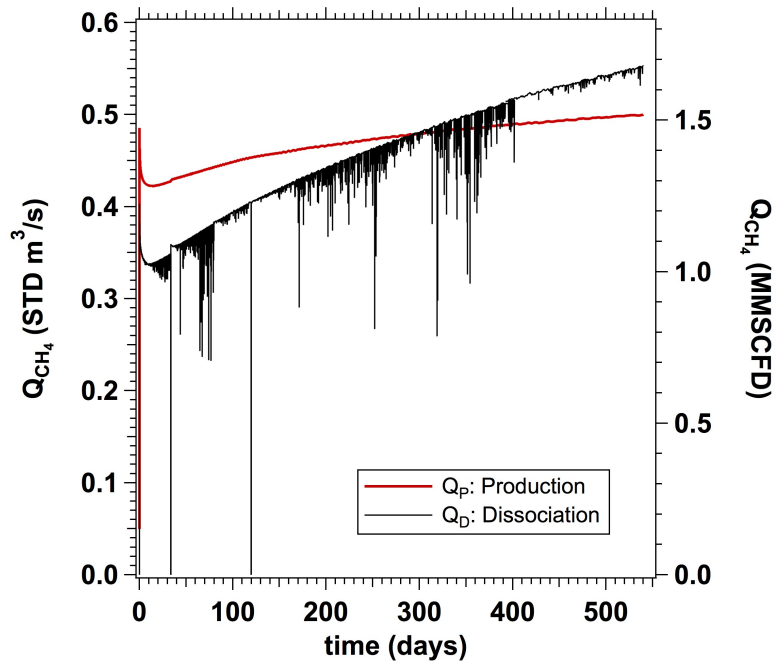
Fig. 3 Evolution of production rate, Q_P, and rate of gas release from hydrate dissociation, Q_R, for Case R1 in both metric (left) and oil industry (right) units.
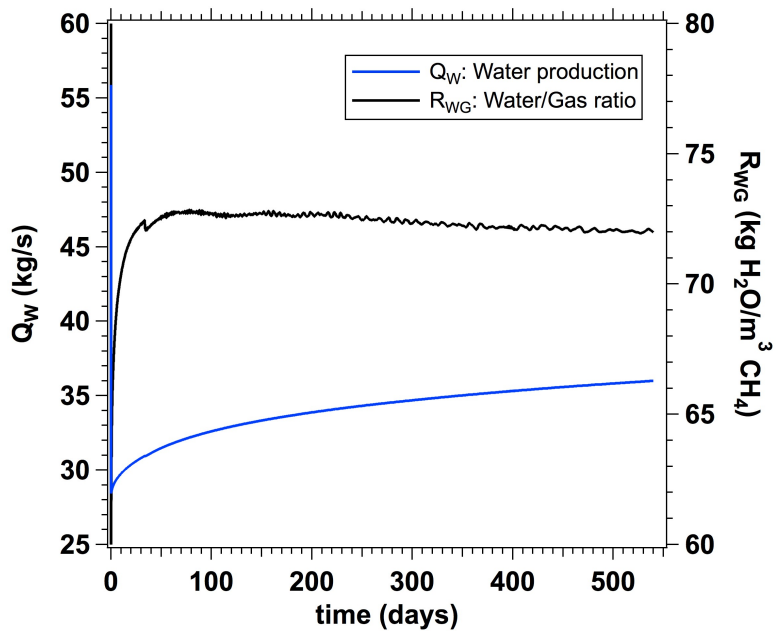

Fig. 4 Evolution of water production, Q_W, and the water-to-gas ratio, R_{WG}, in Case R1.
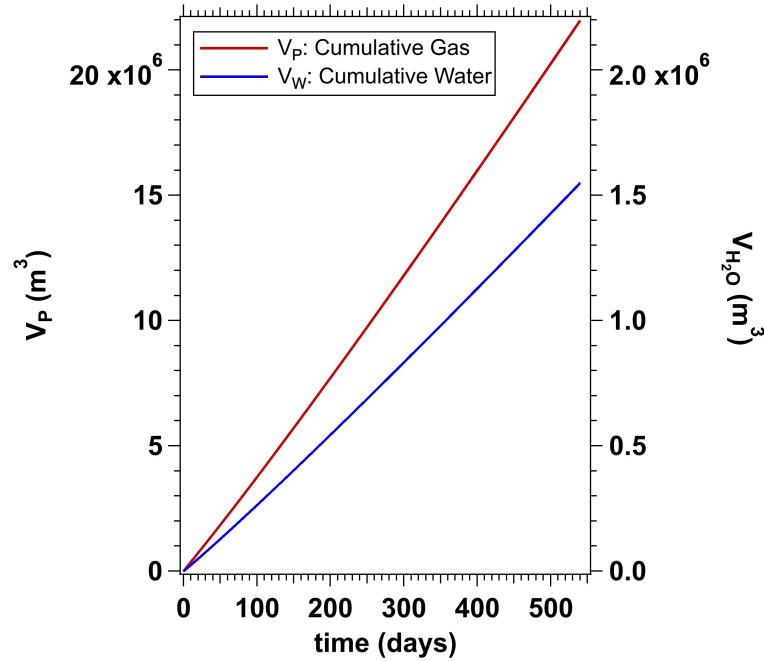
Fig. 5 Evolution of V_P and V_W in Case R1.

The cumulative gas and water production (V_P and V_W, respectively) for Case R1 is shown in Figure 5, and confirm the observations from Figures 3 and 4: the cumulative produced volume V_P in Figure 5 provides further evidence of the significant productivity of the investigated site if targeted for depressurization using a vertical well. After continuous production for $t = 540$ d, $V_P = 22 \times 10^6$ ST m^3($= 7.77 \times 10^8$ ST ft^3) of CH$_4$ are produced. However, the large V_P is accompanied by a very large volume of produced water, $V_W = 1.55 \times 10^6$ m^3.

Also of interest is the evolution of the volume of free gas, V_F, in the reservoir (Figure 6), which increases continuously after onset of production and reaches 1.38×10^7 ST m^3 at the end production, or 63% of the volume of the produced gas V_P. This indicates the formation of a substantial volume of gas in the reservoir that could be accessed later in the production. Also in Figure 6, note that this is of course less than the cumulative volume of gas release through dissociation, V_D. However, comparing Figure 6 to Figure 5, we also note that V_P is similar to, and perhaps very slightly greater, than V_D despite a large quantity of free gas in the reservoir. This is consistent with the production of dissolved methane gas in addition to the production of dissociation-originating gas.

The evolution of water inflows across key boundaries and interfaces at the early stages of production, shown in Figure 7, provides important insights into the overall behavior of the system during production in Case R1 (rates of water inflow stabilize at relatively constant rates at longer time scales). Similarly, water inflows from the ocean floor boundary are zero, though a hydrate reservoir that is closer to the seafloor could perhaps be more likely to interact with overlying ocean during extending production. Inflows through the top of the hydrate reservoir (the top of the H1 layer, see Figure 1) are very small, and there are somewhat larger inflows into the base of the H3 layer via the underlying aquifer (SA). Both of these inflows are dwarfed by water flows into the M2 interlayer through its top and bottom interfaces, representing water flowing from the H2 and H3 HBLs, respectively. This occurs because the low-permeability M2 mud interlayer is more permeable than the hydrate-impregnated H2 and H3 HBLs (low effective permeability due to high hydrate
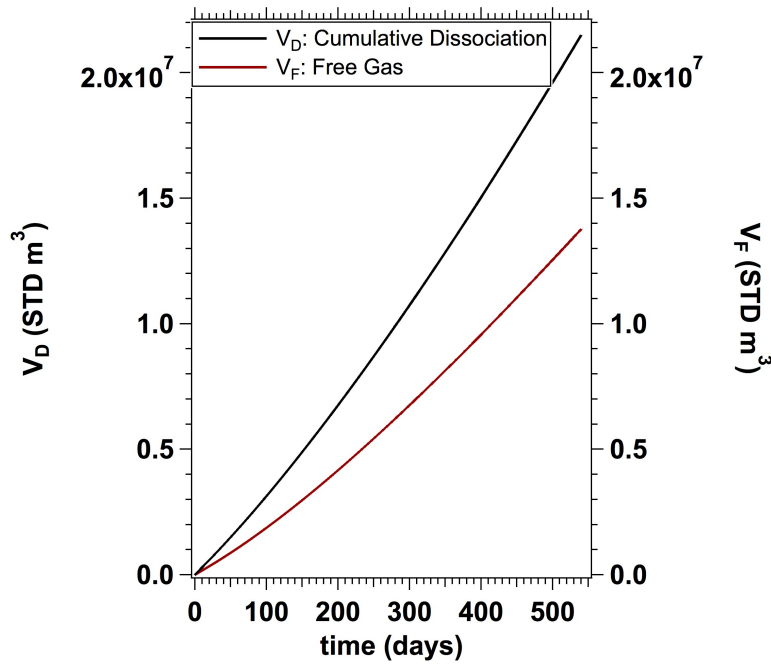
Fig. 6 Cumulative volume of methane released through dissociation, V_D, and the volume of free gas, V_F, for Case R1.

saturation), leading to preferential water flows from the HBLs toward the well through the M2 interlayer rather than along the H2 and H3 layers. For comparison, Figure 7 includes the water production rate Q_W at the well (from Figure 4), from which it can be seen that the M2 interlayer supplies just over 50% of Q_W during the majority of the production period—the remaining water originates mainly from the HBLs (formation water and the products of hydrate dissociation), with a small contribution of water inflow through the base of the H3 HBL.

3.2 Evolution of P, T, S_H, and S_G in Case R1

The spatial evolution of the system during the course of production is described by the color plots in Figures 8 through 11. The evolution of the pressure distribution over time for Case R1 is shown in Figure 8. As expected, the pressure drop, ΔP, is largest across the H1 layer, because of its lower initial $S_H = 0.47$ and consequently higher k_{eff}. The pressure drop is conversely lowest across the H3 layers, due to the higher-S_H (= 0.73) and lower k_{eff} of the H3 layer. Lower pressures in the interlayer above and aquifer below the H3 layer drive the large water flows described by Figure 7. Also note the distinct isolation of the system layers below $z = -250$ m from the depressurization process. The low k_{eff} of the H3 layer shields the deepest (and warmest) hydrate layers from dissociation for several months of production, until hydrate dissociation near the wellbore provides a sufficiently large pathway for communication between the bottom of the H3 layer (and aquifer) and the rest of the reservoir.

The temperature distributions in Figure 9 provide an indication of the locations of hydrate dissociation, as dissociation is an endothermic process, and are consistent with the P-distributions in Figure 8. Thus, the lowest temperatures are associated with the areas of greatest hydrate dissociation, which occurs in the more permeable (lower S_H) H1 and H2 layers. Note the persistence of higher temperature in the H3 layer, and the relative stability of T within the M2 interlayer and
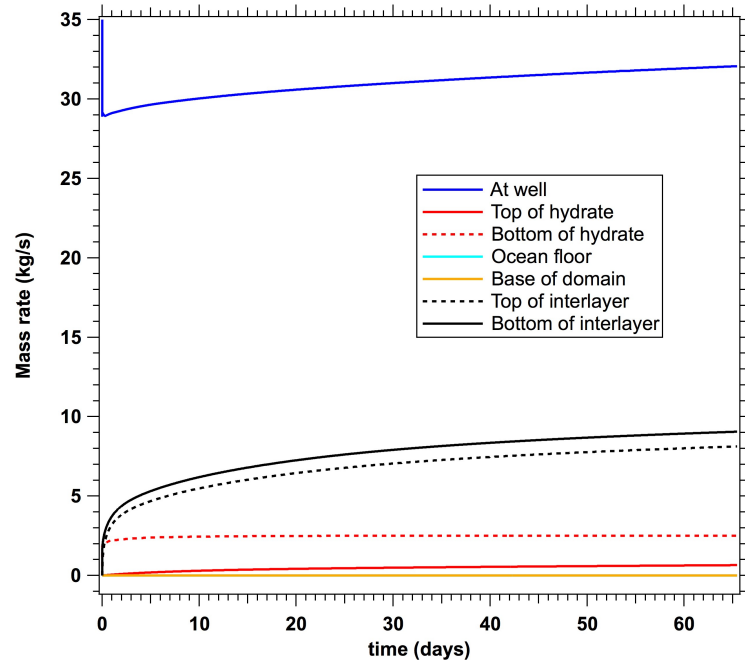
Fig. 7 Evolution of water flows across key boundaries and interfaces, compared to water production at the well, Q_W.
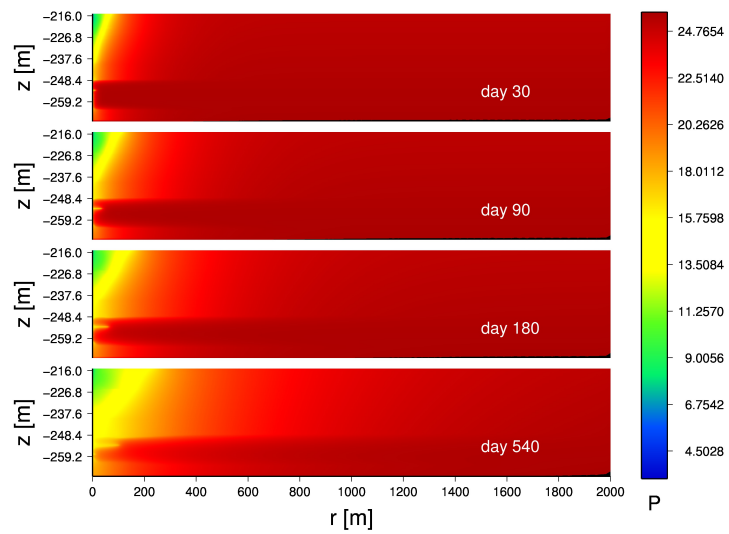

Fig. 8 Evolution of the spatial distribution of pressure (in MPa) in the reservoir of Case R1.
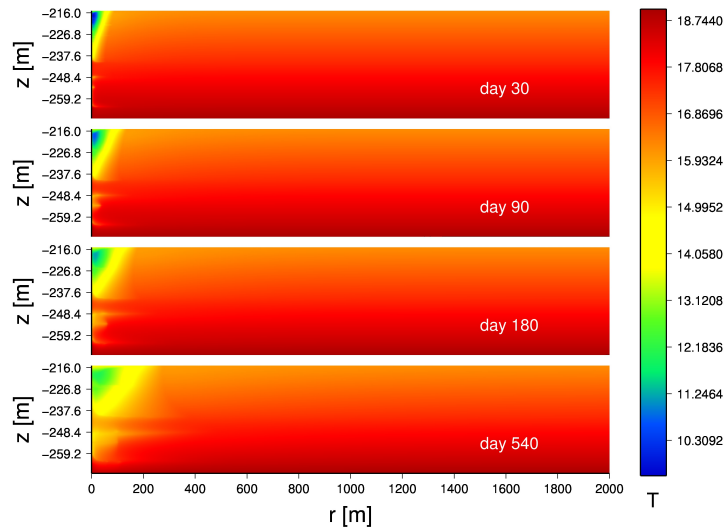
Fig. 9 Evolution of the spatial distribution of temperature (in $^\circ C$) in the reservoir of Case R1.

the SA aquifer where no hydrate is present, no dissociation occurs, and inflows of water are likely to maintain the temperature despite adjacent cooling. As expected, both the extent of depressurization (in Figure 8) and cooling (in Figure 9) expand outward from the wellbore and into the reservoir as time advances.

The evolution of the S_H and S_G distributions are presented in Figures 10 and 11, respectively. They confirm the predictions made from Figures 8 and 9. First the hydrate dissociation is concentrated in the HBLs with the lower-S_H (H1 and H2), while very limited dissociation in evident in the high-S_H H3 layer that remains largely intact. Second, dissociation appears to have affected a small fraction of the main body of the hydrate at the end of the production test (as already indicated by the data in Figure 6), with dissociation limited to a narrow zone around the production intervals and at the bounding surfaces of the three hydrate layers. The S_G distributions show gas accumulating in the upper layers of the system, because (1) the higher k_{eff} at these locations causes more intense depressurization-induced dissociation and because (2) of the buoyancy of the free gas. Also note that gas saturations are noticeably higher at and along the boundaries of the HBLs, due to increased permeability in the interlayers and in the aquifer leading to more widespread depressurization (depressurized front travels further) and enhanced dissociation and gas accumulation at these locations.

3.3 Geomechanical system response

The geomechanical formulation described in Part 2 of this series was used to simulate the geomechanical response of the system during production. This simulation was performed on the mesh shown in the bottom of Figure 2. The mesh has 11,542 nodes and 11,378 elements, 23,084 displacement degrees of freedom (which dictates the size of the linear system of equations), and 182,048 additional stress degrees of freedom (four components per four quadrature points per element) that are stored and updated. "Roller" boundary conditions (i.e. no displacement normal to the boundary) on three sides of the 2D domain: the center axis at the left of the domain (well location) has vertical rollers for the axisymmetric boundary condition, the right of the domain also has vertical rollers, and the bottom of the domain has horizontal rollers to confine the system. The top of the domain has a boundary condition of an applied normal traction (equal to the pressure). The
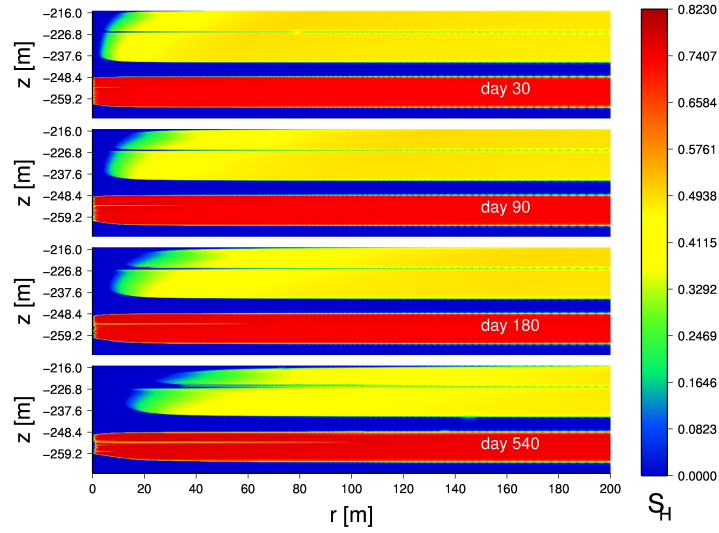
Fig. 10 Evolution of the spatial distribution of S_H in the reservoir of Case R1.
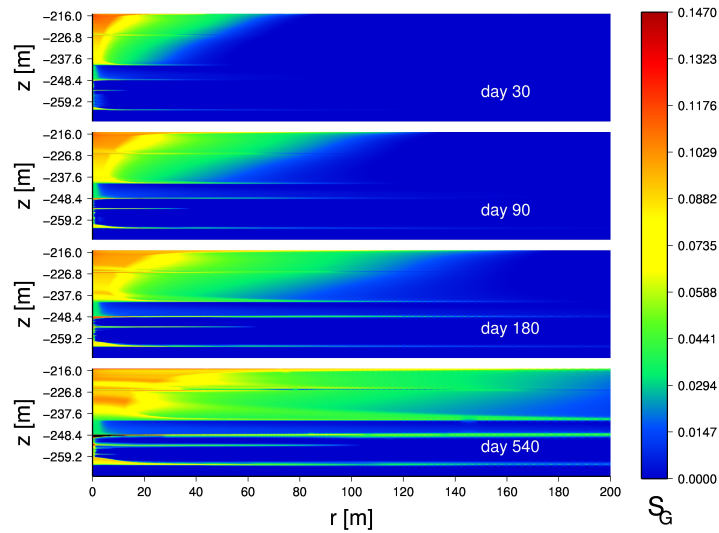

Fig. 11 Evolution of the spatial distribution of S_G in the reservoir of Case R1.

unstructured geomechanics mesh is coupled to the rectilinear thermal-hydrological mesh via the methodology described in Part 2, where a mapping between the separate meshes is generated at simulation start, allowing properties to be projected/interpolated between simulators.

The mechanical state of the system after 540 days of production is shown for the entire domain in Figure 12, with a magnified view of the production zone at different points in time shown in Figure 13. The time history of vertical displacement state at three key locations in the system (seafloor, top of hydrate bearing layer, bottom of hydrate bearing layer) is shown in Figure 14. The drop in pore fluid pressure due to production causes the reservoir to contract. The top of the topmost hydrate layer and bottom of the bottommost hydrate layer exhibit the maximum subsidence and uplift, respectively. It can also be seen that the reservoir contracts radially towards the wellbore, as
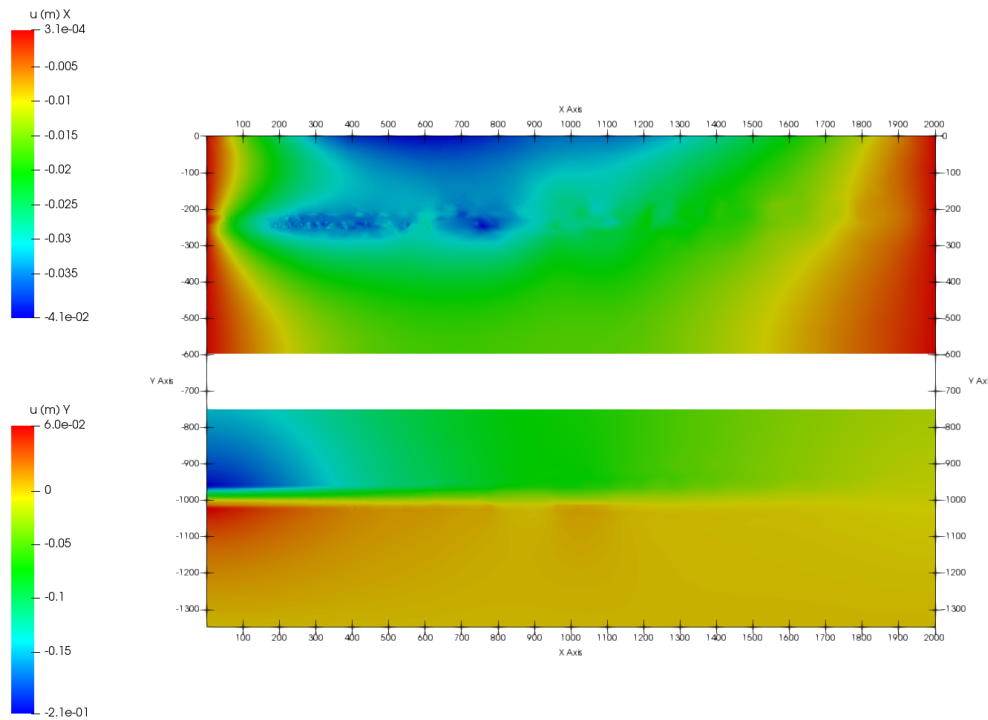
Fig. 12 Displacement fields for the entire domain (seafloor to domain bottom) at $t = 540$ days. The vertical displacement (labeled as Y) is shown on the bottom, and the radial displacement (labeled as X) is shown on the top. The coloring and axis labels are scaled by meters. The domain is drawn twice in the same scene, so that the vertical displacement color plate starts with $0m$ shifted down to $-750m$.

shown in Figure 13. Due to the displacement boundary at the bottom of the domain, the drop in total stress inside of the reservoir pulls the underburden upwards, causing uplift along the bottom of the hydrate layers. As production continues, the entire reservoir subsides, which causes the "point of pinching" along the height of the wellbore observed in Figure 13 to move downwards.

In Figure 15 we compare the gas production predicted by both the fully-coupled and flow-only simulations. Evolution of production is similar in both cases, however, we see a reduction in production rate for the case without coupled geomechanics. An interesting effect in the hydrate dissosociation is noticed in Figure 16 that is quantitatively exampled through a cross section plot of pressure, hydrate saturation, and permeability in Figure 17. With geomechanics, the lower H3 HBL shows lensing behavior (alternating vertical layers of high and low saturation) and limited dissociation next to the well, whereas without solving the geomechanical problem, wormholes (i.e., the irregular zone near the well and the horizontal open pathway at $z = -251$ m) develop and dissociation proceeds heterogeneously away from the well. No major differences are seen in the upper two hydrate layers, which initially have $S_H = 0.4$, less than the initial saturation of $S_H = 0.73$ for the lower H3 HBL. Clearly the inclusion of geomechanics has a strong effect on the reservoir evolution. Our preliminary conclusion in this particular case is that the geomechanical response changes the evolution of effective permeability in the high-S_H zones (which can be very low initially), allowing a
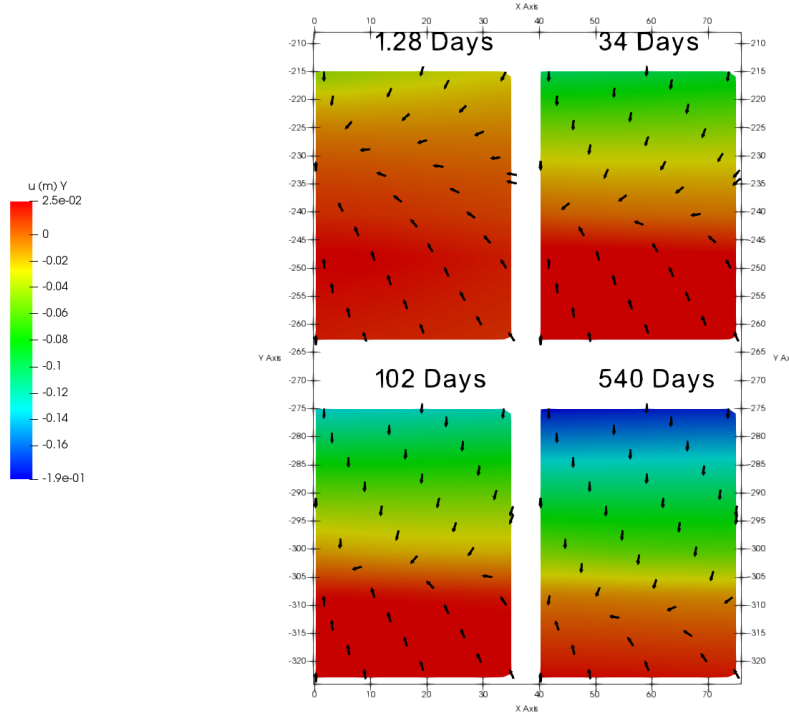
Fig. 13 Displacement fields near the well in the hydrate layers at 1.28, 34, 102, and 540 days. The arrows denote the direction of the displacement. The background is colored by the total vertical displacement, scaled in meters. Similarly to the previous figure, the top left color plate is in the correct position with respect to the axis, and the three color plates are shifted by 40 m to the left and 60 m down to form a grid in the Paraview scene.

more effective dissociation response to depressurization. Simulated depressurization of high-S_H, low k_{eff} hydrate zones, when simulated without geomechanical response, has suggested the formation of self-sharpening dissociation fronts with localized increases in S_H and wormholing behavior. Such increases in S_H and the corresponding effect on k_{eff} can be observed in Figure 16. With fully-coupled geomechanics, this behavior is not seen. This observation warrants further investigation in future simulation studies of the complex interactions between the geomechanical response and the dissociation and flow patterns. However, the interactions between geomechanical responses and the evolution of hydrate saturation are complex, and we cannot assume any universal trend based on these results.

3.4 Sensitivity Analyses – Case R1

We investigated the sensitivity of gas production to the following variations in reservoir parameters:

(a) Case R1n: The effective permeability k_{eff}, as controlled by the exponent n in the k_{rel} equation (see Table 1). The value of n is reduced from $n = 4.30$ in Case R1 to $n = 2.36$, resulting in $k_{eff} = 1 \times 10^{-14}$ m^2($= 10$ mD), an increase by a factor of 1,000 over Case R1.

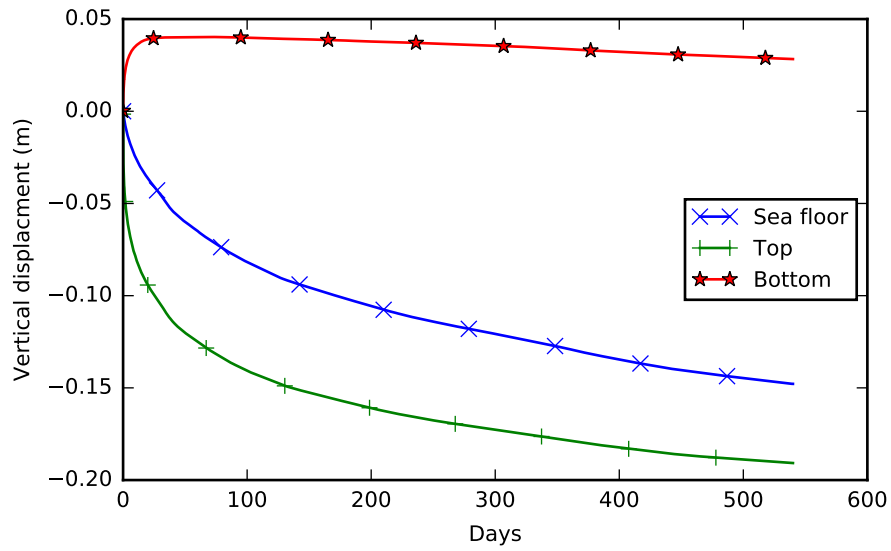(b) Case R1th: The wet (fully saturated) thermal conductivity is increased to $k_{\theta W} = 3.0$ W/m/K

Fig. 14 Vertical displacement history at three locations along the well at $r = 0$: the seafloor ($z = 0.0$m), the top of the hydrate bearing layer ($z = -214.9$m), and the bottom of the hydrate bearing layer ($z = -263.6$m).
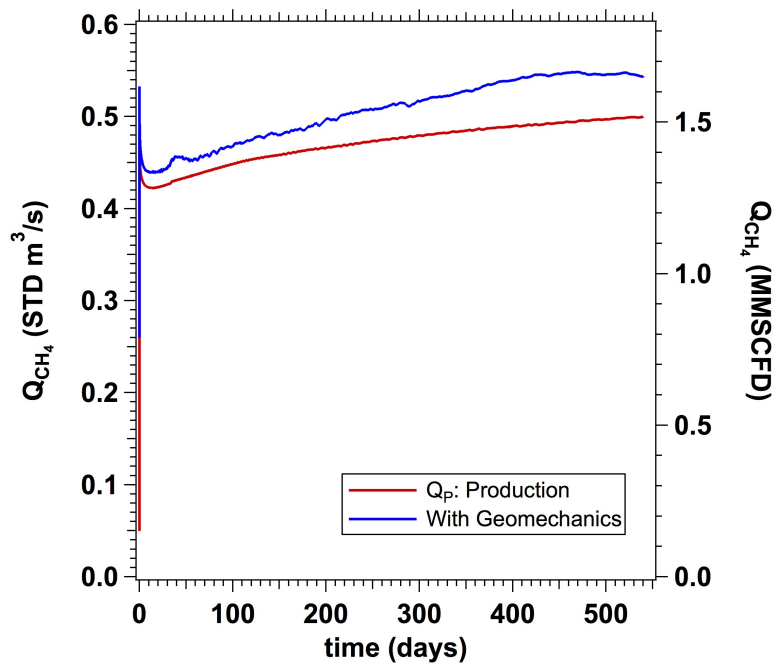

Fig. 15 Gas production over time calculated with and without the fully-coupled geomechanical formulation; i.e., with Millstone solving the fully-coupled geomechanical response vs. only using simplified pore compressivities with TOUGH+.
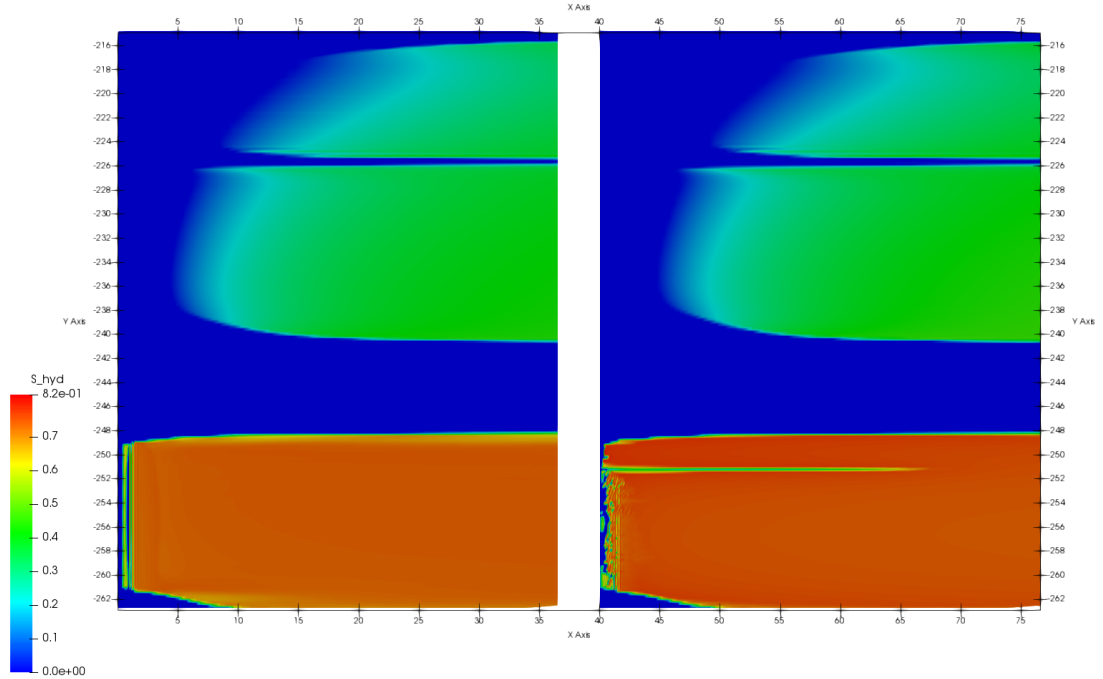
Fig. 16 Comparison of methane hydrate distribution in the hydrate bearing layers of the reservoir at 90 days with fully-coupled geomechanics on the left, and without geomechanics on the right. The distributions in the top two H1 and H2 layers are are similar, but the mode of dissociation is very different in the bottom-most H3 layer which initially has a higher saturation. Lensing appears with fully-coupled geomechanics, and wormholing appears with the simplified pore-compressivity relations.

(c) Case R1w1: The length of the well is reduced by 5.5 m, i.e., the bottom of the well in this case is 5.5 m above the base of the H3 HBL and thus further from the underlying permeable aquifer

Figure 18 shows the Q_R and Q_P for Cases R1, R1n, and R1th, and Figure 19 shows the corresponding cumulative produced gas, V_P, and produced water, M_W. As expected, the much higher k_{eff} in case R1n results in a much larger Q_P and M_W (but less than double of that in case R1), but Q_R is lower because the higher k_{eff} results in less effective depressurization due to increased inflows of water. This indicates a larger contribution of dissolved gas to Q_P than in the R1 Case, since the only sources of producible gas within the reservoirs are dissociating hydrate or gas dissolved in formation water and exsolved due to the rapid decrease in pressure. Conversely, the increased thermal conductivity in Case R1th enhances the rate of hydrate dissociation, Q_R, and also increases the rate of gas production, Q_P, although the enhancement of production is not nearly as significant as seen in the high-permeability Case R1n.

Cumulative gas production, seen in Figure 19, tracks production rate for all three cases. Cumulative produced water, also shown in Figure 19, also increases with the increased HBL effective permeability in Case R1n, while the increased rate of hydrate dissociation in Case R1th does not change the amount of produced water significantly compared to the reference case. The behavior of the reference case is likely due to formation water dominating as the source of produced water.
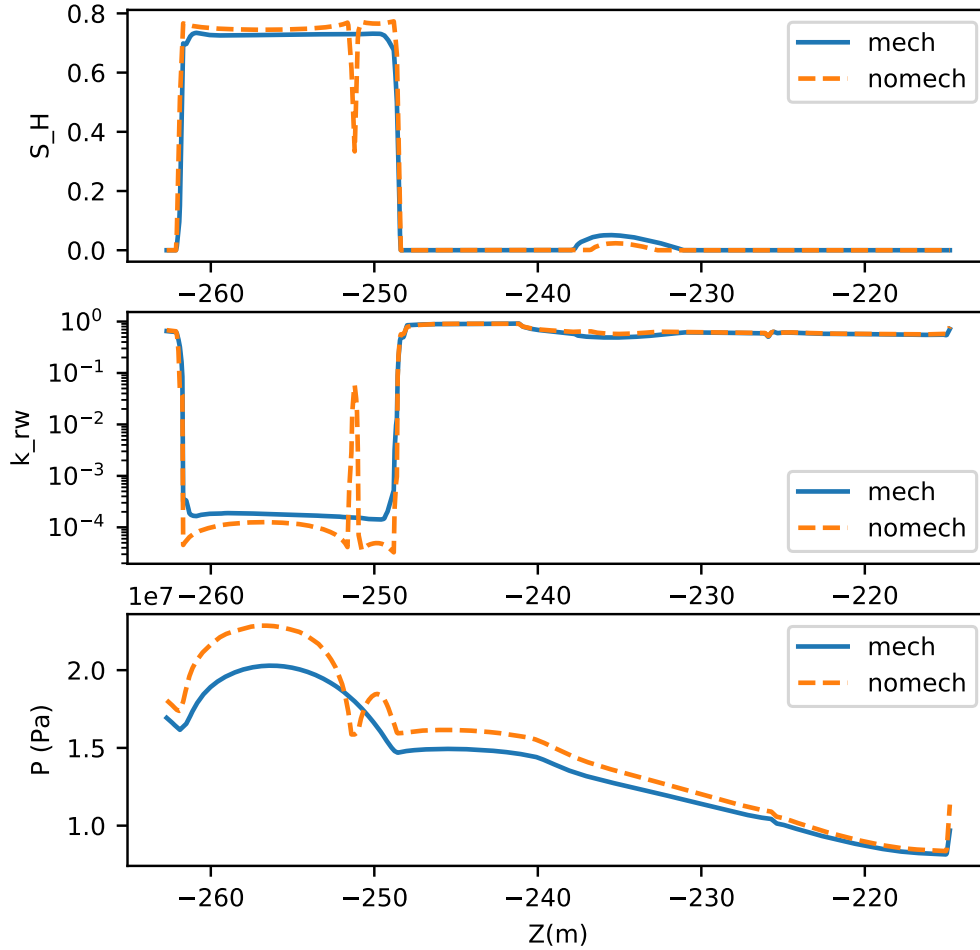
Fig. 17 Comparison of the reservoir state at 90 days through a vertical cross section 5 m away from the borehole (along $x = 5$ and $x = 5 + 40$ vertical slices in the Figure 16) for the hydrate saturation S_H, relative water permeability k_rw, and pore pressure P. The bottom of the H3 layer starts on the left side of the axis, going upwards until the top of the H1 layer on the right side of the axis. The key "mech", solid line, corresponds to the fully-coupled simulation, and "no mech" corresponds to the simplified geomechanical models in the flow only simulation. The relative permeability is plotted on a log-scale in the vertical axis to highlight the bottom low-permeability layer.

In Figure 20, Case R1n exhibits a much higher R_{WG} than in Case R1. Increased effective permeability of the HBLs assists transport of water from the boundaries, but such water can also carry dissolved gas that can exsolve and be produced; thus, increased Q_P despite decreased Q_R. The higher $k_{\theta W}$ in Case R1Th leads to increased Q_R and Q_P because of more efficient heat transport, which leads to enhanced dissociation yet a reduction in R_{WG} as the additional water originates from dissociation rather than increased inflow from the boundaries.
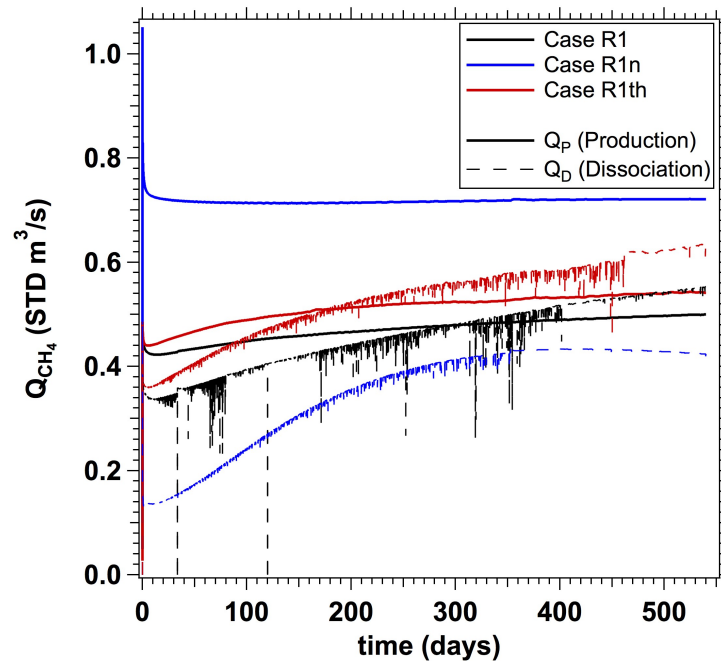
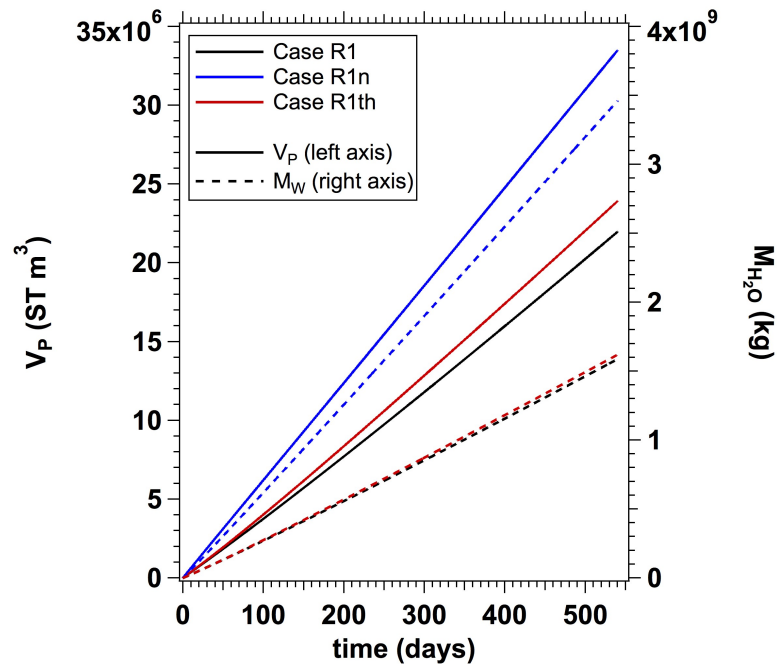**Fig. 18** Comparison of the evolution of Q_P and Q_R in Cases R1n and R1Th to those in Case R1.

Fig. 19 The evolution of V_P and M_W in Cases R1n and R1Th vs. Case R1.
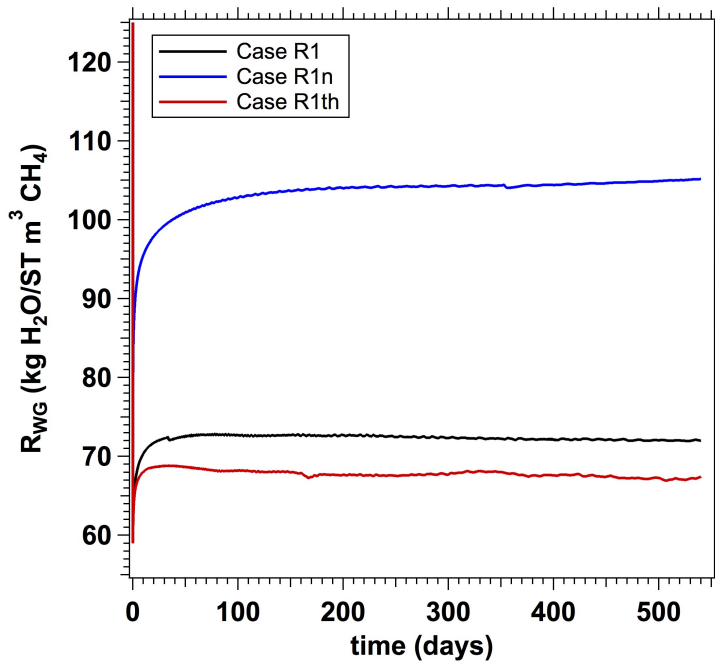
Fig. 20 Comparison of the evolution of R_{WG} in Cases R1n and R1Th to that in Case R1.

The effect of the shorter well in Case R1w1 is depicted in Figures 21 and 22. Figure 21 describes the evolution of Q_R and Q_P, and shows that the reduced length enhances both hydrate dissociation and gas production. This is because the greater separation from the aquifer by low-permeability hydrate-bearing layers at the base of the H3 HBL reduces water flows from the higher-permeability aquifer and more effectively concentrates depressurization and dissociation in that layer. This is confirmed in Figure 22, where both Q_W and R_{WG} are lower for Case R1w1 than in Case R1, although both are still high in absolute terms.

3.5 Response of a multi-well system (Case CS1) to production

As discussed earlier, Case CS1 describes the behavior of a single vertical well that is part of a system of multiple wells deployed on a regular grid with a well spacing of 300 m. This is achieved by truncating the existing mesh to a maximum radius of $r = 150$ m and applying a no-flow boundary at that radius. This assumes that wells in the center of such a field are protected from lateral inflows of water by other wells, thus providing us with an idealized upper-bound on potential single-well productivity.

Figure 23 shows the evolution of Q_R and Q_P over time, and shows the effect of the no-flow boundaries in Case CS1: both Q_R and Q_P are initially substantially higher than those for the reference case. The no-flow boundary at $r = 150$ m results in a smaller reservoir volume subject to depressurization and no risk of water inflows from the outer boundary. This leads to more effective depressurization, stronger hydrate dissociation rates, and larger production rates. Compared to the reference case, however, the volume of the reservoir accessed by each particular well is smaller and exhausted more quickly, as evidenced by the decline in the free gas volume V_F in the reservoir in Figure 24(left) after $t = 100$ d. The higher Q_P of Figure 23(right) is translated into the higher produced volume V_P in Figure 24(right). Of particular interest is the evolution of the Water-to-Gas
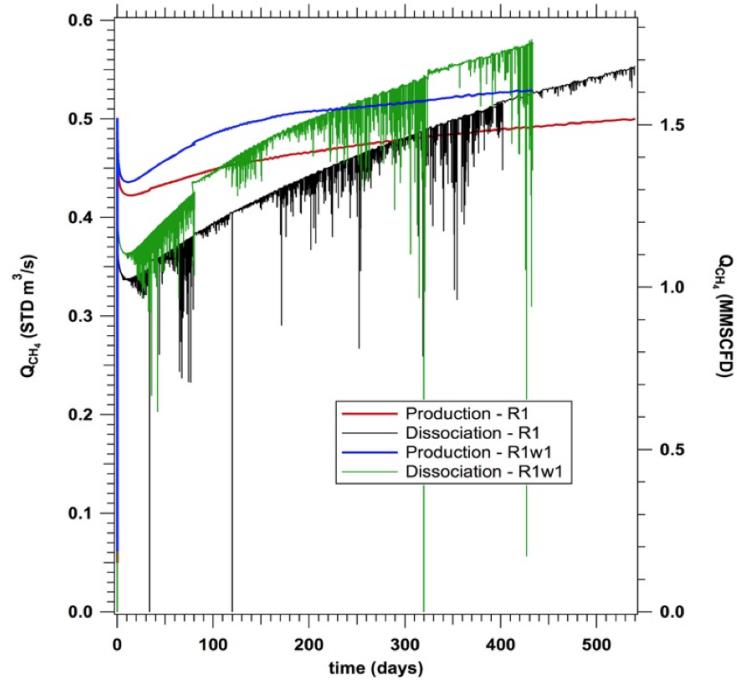
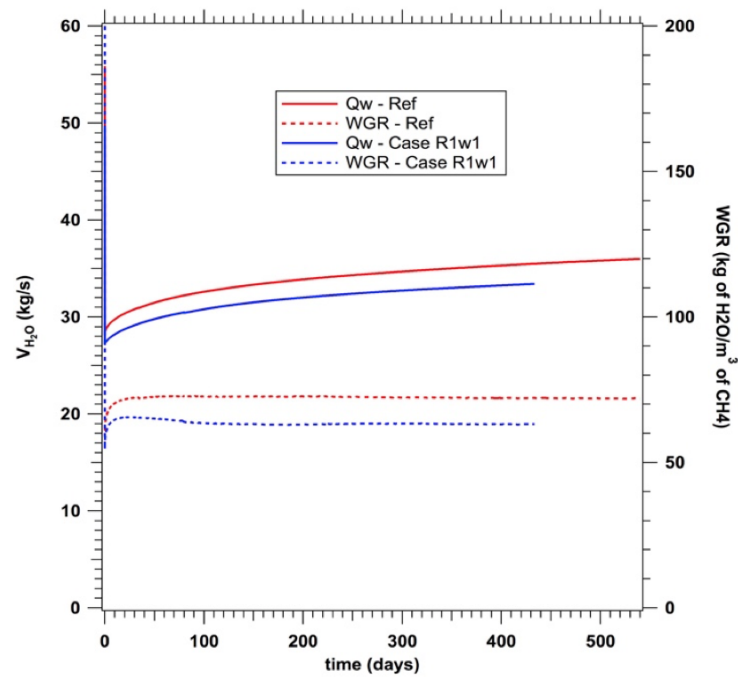**Fig. 21** Comparison of the evolution of Q_P and Q_R in Case R1w1 to that in Case R1.

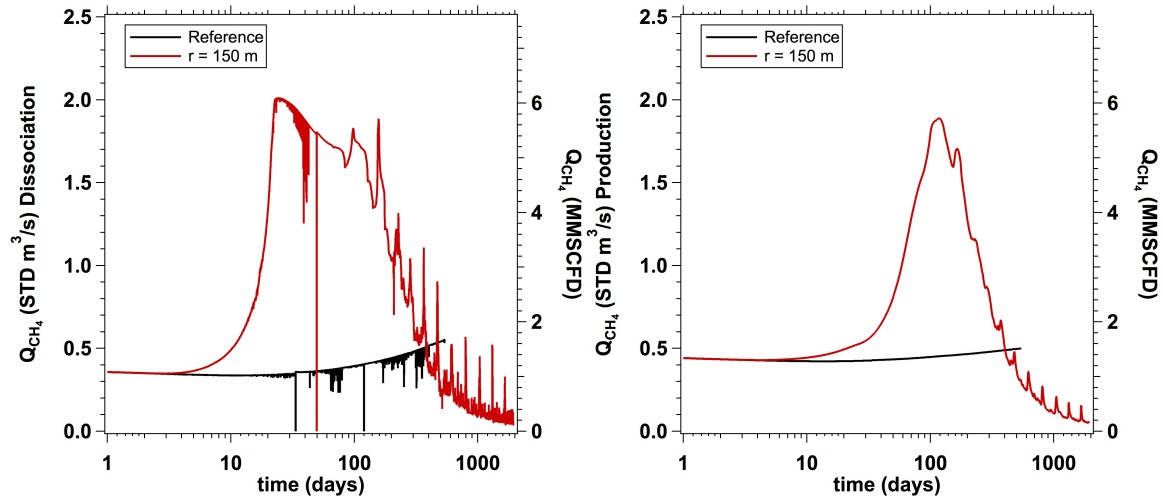**Fig. 22** Comparison of the evolution of Q_W and R_{WG} in Case R1w1 to that in Case R1.

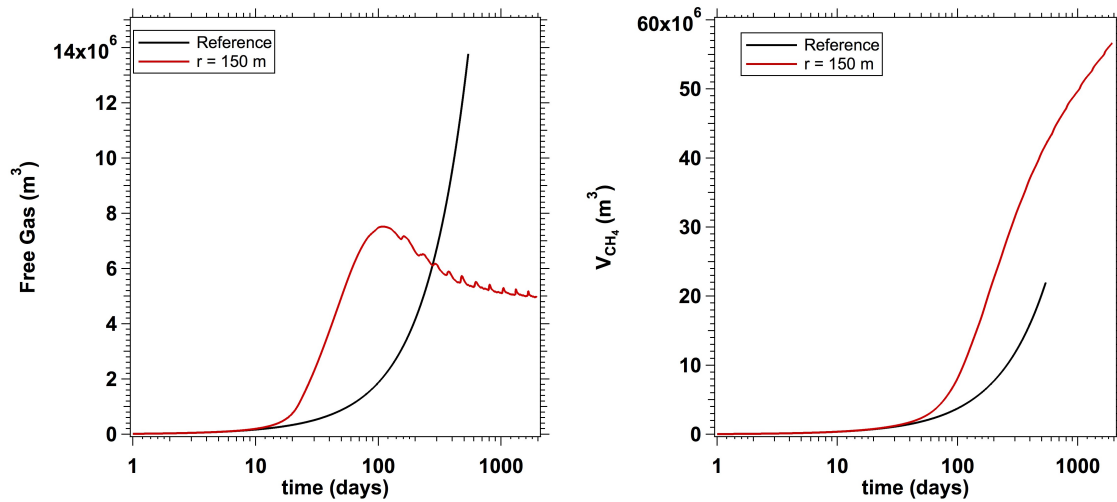**Fig. 23** Evolution of Q_R (left) and Q_P (right) in Case CS1.

Fig. 24 Evolution of V_F (left) and V_P (right) in Case CS1.

ratio R_{WG} in Figure 25, which shows a rapid decline beginning 10 days from the onset of production and reaches a low-level plateau of 4.0 after $t = 100$ d. This is caused by the elimination of water inflows from permeable horizontal boundaries in the closed system, and the plateau is maintained for a long time until the hydrate resource is exhausted.

4 Conclusions

In this series, we document the development and use of the TOUGH+Millstone simulator, which involves a coupling of the fully implicit TOUGH+HYDRATE v2.0 (T+H) simulator, describing flow, thermal, and chemical processes in hydrate-bearing media, with the Millstone v1.0 geomechanical model to describe the corresponding geomechanical response. We describe in detail the overall capabilities and the concepts, physics, constitutive relationships, correlations, parameters and com-
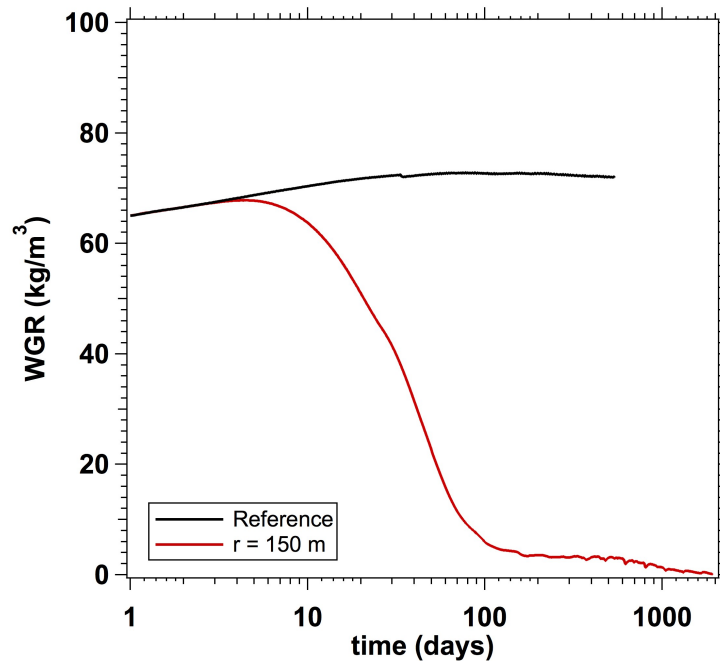
Fig. 25 Evolution of R_{WG} in Case CS1.

putational approaches that are incorporated in the T+H and the Millstone codes, which account for the most recent advances in all known flow, thermophysical and geomechanical processes.

In this paper, the third part of the series, we demonstrate the capabilities of the TOUGH+Millstone simulator in the analysis of the production performance of a complex, multilayered system of hydrate-bearing sediments in an oceanic environment, including its geomechanical response. New models were incorporated into TOUGH+Hydrate to tackle a wider range of phenomena crucial to describe real-world field sytems, as described in Part 1 of this series. Because no preexisting geomechanical coupling was able to solve this class of problems, new numerical algorithms were developed and implemented in the new Millstone geomechanical simulator, described in Part 2 of this series. The study of the example provides an insight into the complexity of the behavior of hydrate-bearing systems, and the interdependence of the flow, thermal, chemical, and geomechanical processes that cannot be approximated by simplifying assumptions. In particular, the presence of closed or relatively impermeable boundaries (top, bottom, and horizontally) is crucial to 1) allow effective depressurization-induced dissociation and 2) limit water inflow and water production. Such impermeable boundaries are achieved via a low-permeability overburden and underburden and also via a pattern of multiple wells that prevent water incursion from the lateral boundaries. Without such protections, high water-to-gas ratios may result in a reservoir becoming impractical for long-term production.

While the properties of this system lead to moderate subsidence and compaction, the effects of including geomechanical response are still noticable, both in the spatial evolution of the system, the location and degree of hydrate dissociation, and the simulated productivity of the system. There are significant differences between the fully-coupled geomechanical model, using the full solution of the stresses and displacements using finite elements, and the simplified models, using single-gridblock pore-compressibility relations.

Acknowledgments

References

G. J. Moridis. User's manual for the hydrate v1.5 option of tough+ v1.5: A code for the simulation of system behavior in hydrate-bearing geologic media,. Technical Report LBNL-6871E, Lawrence Berkeley National Laboratory, 2014.

G. J. Moridis. User's manual of the meshmaker v1.5 code: A mesh generator for domain discretization in simulations of the tough+ and tough2 families of codes. Technical Report LBNL-1005134, Lawrence Berkeley National Laboratory, 2016.

G. J. Moridis and K. Pruess. User's manual of the tough+ v1.5 core code: A general purpose simulator of non-isothermal flow and transport through porous and fractured media. Technical Report LBNL-6869E, Lawrence Berkeley National Laboratory, 2014.

G. J. Moridis and M. T. Reagan. Gas production from oceanic class 2 hydrate accumulations. In *Proc. Offshore Technology Conference*, Houston, Texas, May 2007a.

G. J. Moridis and M. T. Reagan. Strategies for gas production from oceanic class 3 hydrate accumulations. In *Offshore Technology Conference*, Houston, Texas, May 2007b.

G. J. Moridis, M. B. Kowalsky, and K. Pruess. Tough+hydrate v1.0 user's manual: A code for the simulation of system behavior in hydrate-bearing geologic media. Technical Report LBNL-0149E, Lawrence Berkeley National Laboratory, 2008a.

G. J. Moridis, M. B. Kowalsky, and K. Pruess. Depressurization-induced gas production from class 1 hydrate deposits. *SPE Reservoir Evaluation and Engineering*, 10(5):458–488, 2008b.

G. J. Moridis, J. Kim, M. T. Reagan, and S. j. Kim. Feasibility of gas production from a gas hydrate accumulation at the ubgh2-6 site of the ulleung basin in the korean east sea. *Journal of Petroleum Science and Engineering*, 108:180–210, 2013. doi: 10.1016/j.petrol.2013.03.002.

G. J. Moridis, M. T. Reagan, A. F. Queiruga, and R. Boswell. Evaluation of the performance of the oceanic hydrate accumulation at site nghp-02-09 in the krishna-godavari basin during a production test and during single and multi well production scenarios. *Marine and Petroleum Geology*, 2018. doi: 10.1016/j.marpetgeo.2018.12.001.

W.F. Waite, J. Jang, T.S. Collett, and P. Kumar. Downhole physical property-based description of a gas hydrate petroleum system in nghp-02 area c: A channel, levee, fan complex in the krishna-godavari basin offshore eastern india. *Marine and Petroleum Geology*, 2018. ISSN 0264-8172. doi: https://doi.org/10.1016/j.marpetgeo.2018.05.021. URL `http://www.sciencedirect.com/science/article/pii/S0264817218302241`.

K. Zhang, G. J. Moridis, Y. S. Wu, and K. Pruess. A domain decomposition approach for large-scale simulations of coupled processes in hydrate-bearing geologic media. In *6th International Conference on Gas Hydrates*, pages 6–10, Vancouver, British Columbia and Canada, July 2008.